ADVANCED MATERIALS INTERFACES
Open Access
www.advmatinterfaces.de

Tunable Encapsulation and Doping of Monolayer MoS_2 by In Situ Probing of Excitonic Properties During Atomic Layer Deposition

Alex Henning, Sergej Levashov, Chenjiang Qian, Theresa Grünleitner, Julian Primbs, Jonathan J. Finley, and Ian D. Sharp**

Here, it is shown that in situ spectroscopic ellipsometry (SE) is a powerful method for probing the effects of reactant adsorption and film formation on the excitonic properties of 2D materials during atomic layer deposition (ALD), thus allowing optimization of both film growth and opto(electronic) characteristics in real time. Facilitated by in situ SE during ALD on monolayer MoS_2, a low temperature (40 °C) process for encapsulation of the 2D material with a nanometer-thin alumina (AlO_x) layer is investigated, which results in a 2D/3D interface governed by van der Waals interactions rather than chemical bonding. Charge transfer doping of MoS_2 by AlO_x is found to be an interfacial phenomenon that initiates from the earliest stages of film formation, but saturates upon deposition of a closed layer. However, the lack of chemical binding interactions at the 2D/3D interface enables physical removal of the AlO_x that results in a reversal of the charge transfer doping effect. Overall, it is demonstrated that in situ SE of 2D materials during ALD can precisely probe the impact of film formation on sensitive optoelectronic characteristics of 2D materials, which is of key importance in the development of integrated 2D/3D systems.

1. Introduction

2D layered materials are attracting intensive interest in fundamental and applied science, with groundbreaking performance characteristics achieved in applications across different fields, including catalysis,[1] photonics,[2] optical sensing,[3] and more-than-Moore (MtM) electronics.[4] Because 2D van der Waals (vdW) semiconductors retain a high carrier mobility even at the monolayer limit, where short channel effects are largely suppressed, they may replace or augment silicon (Si) to overcome scaling and performance limitations of current semiconductor technologies.[5] However, few- and single-layer 2D materials are supremely sensitive to their dielectric environments, which must be controlled on the atomic level in a scalable manner to make full use of their intrinsic properties in optical and electronic device applications.[4] This represents a considerable challenge, since most conventional techniques used for dielectric or metal integration in semiconductor technology, such as high-temperature oxidation, sputtering, evaporation, and chemical vapor deposition (CVD), can degrade the 2D crystal as a consequence of high energy atoms impacting the surface[6] or gas-phase reactants interacting with the 2D material at elevated temperatures. In contrast, atomic layer deposition (ALD) relies on the sequential injection of gas-phase reactants into a reactor chamber at moderate temperatures (<300 °C) and provides a delicate route to the controlled and large-scale deposition of thin films on sensitive substrates.

Although ALD offers considerable advantages for 2D/3D materials integration, conformal deposition on 2D materials without the introduction of defects has proven to be challenging due to the lack of reactive sites on the fully coordinated basal planes of vdW materials.[7] For the realization of continuous and ultrathin coatings by ALD, seed layers on 2D nanosheets have been demonstrated to facilitate nucleation and yield uniform ALD coatings,[8] but their application is incompatible with large-scale manufacturing and may reduce interface stability during device operation. As an alternative, gas-phase surface activation prior to or during ALD, including (UV) ozone treatment[7a,9] or plasma-assisted approaches,[10] can be easily combined with the growth process. However, such treatments can be deleterious to the 2D crystal and introduce additional defects.[11] In this regard, there is a pressing need to understand the evolution of the optoelectronic characteristics of 2D materials during growth of films on their surfaces, and especially during the critical stage of nucleation when the basal plane is exposed to the reactive gas environment.

Despite the importance of the initial growth regime in defining both interface and film, in situ investigations during

A. Henning, S. Levashov, C. Qian, T. Grünleitner, J. Primbs, J. J. Finley, I. D. Sharp
Walter Schottky Institute and Physics Department
Technical University of Munich
85748 Garching, Germany
E-mail: alex.henning@wsi.tum.de; sharp@wsi.tum.de

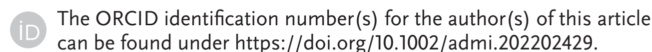
The ORCID identification number(s) for the author(s) of this article can be found under https://doi.org/10.1002/admi.202202429.

© 2023 The Authors. Advanced Materials Interfaces published by Wiley-VCH GmbH. This is an open access article under the terms of the Creative Commons Attribution License, which permits use, distribution and reproduction in any medium, provided the original work is properly cited.

DOI: 10.1002/admi.202202429

 © 2023 The Authors. Advanced Materials Interfaces published by Wiley-VCH GmbH

ALD on 2D materials are largely missing. With few exceptions,[12] film nucleation on 2D materials has been studied by transferring the sample to an analysis chamber and characterizing the surface after ALD (half)cycles.[7b,13] While this approach has provided important mechanistic insights into growth, it is less suitable for understanding interactions of the 2D material within reactive environments or for rapid development of complex growth processes. Here, we address this gap via the implementation of in situ spectroscopic ellipsometry (SE) during ALD to gain real-time insights into film nucleation on the 2D surface, while simultaneously probing the impact of the adlayer on the dielectric function and excitonic properties of the 2D material. We use this approach to enable encapsulation of CVD-grown monolayer MoS_2 with a continuous and nanometer-thin aluminum oxide (AlO_x) layer using trimethylaluminum (TMA) in combination with ozone at 40 °C. The low temperature of the process facilitates nucleation[13a,14] due to physical adsorption of TMA on MoS_2[15] and minimizes crystal defect creation in the 2D layer.

We find that the optoelectronic characteristics of 2D monolayers are highly sensitive to film formation, with adlayer charge transfer (or defect modulation doping)[8d,16] starting from the very first ALD cycle and increasing during several successive cycles. However, film-induced changes to excitonic absorption saturate following the formation of a nanometer-thin alumina coating, confirming that charge transfer doping is defined by the abrupt interface. Complementary ex situ elemental analysis by X-ray photoelectron spectroscopy (XPS), as well as combined atomic force microscopy (AFM) and optical spectroscopy measurements, indicate the formation of a weakly interacting alumina layer that is physisorbed on MoS_2. In addition to introducing *n*-type doping in monolayer MoS_2 via adlayer charge transfer,[8d,16a] we find that a continuous ≈18 Å-thin AlO_x film protects the 2D material and enables metallization while suppressing defect formation, which is of relevance for fabrication of tunneling contacts. Thus, this study provides a new route for tailoring the electronic properties at 2D/3D interfaces via low-temperature ALD, along with a generalizable approach to understanding film formation and accelerating process development by means of in situ SE at early stages of growth.

2. Results and Discussion

To investigate film deposition in real time, we utilized the experimental configuration illustrated in **Figure 1**a, which comprises an in situ spectroscopic ellipsometer coupled to an ALD chamber equipped with an ozone generator. Using SE, we measured the changes in phase, Δ, and amplitude, Ψ, from the incident polarized light reflected off a Si substrate

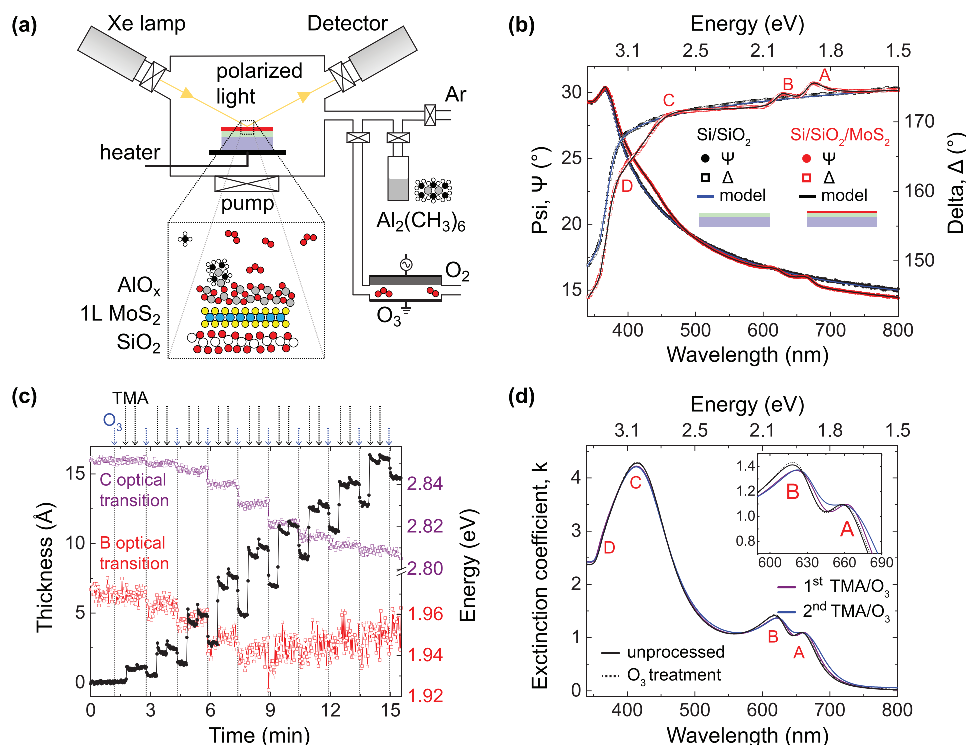

Figure 1. In situ spectroscopic ellipsometry of monolayer MoS_2 during ALD. a) Schematic illustration of the ALD setup, including in situ spectroscopic ellipsometry light source and detector, and the sample structure. b) Representative Ψ and Δ spectra of a bare Si/SiO_2 substrate (black circles and squares) and a monolayer MoS_2 covered substrate (red circles and squares). The inset shows the two structures used to model the measured data. The positions of the MoS_2 A, B, C, and D exciton features are indicated. c) Real-time monitoring of the adlayer thickness on MoS_2 during the TMA/O_3 process at 40 °C (black line and circles, left axis) and simultaneous changes of the MoS_2 B- and C-exciton absorption energies (right axis). d) Plots of the extinction coefficient as a function of wavelength for monolayer MoS_2, extracted from the analysis of SE data, following different in situ treatments. The inset shows a zoom-in of the spectral region in the range of the A- and B-exciton optical transitions.

 © 2023 The Authors. Advanced Materials Interfaces published by Wiley-VCH GmbH

covered with monolayer MoS_2 (Figure 1b) in the spectral range from 340 to 1700 nm. Continuous monolayers of MoS_2 (Figure S1, Supporting Information) with lateral dimensions larger than the spot size of the focused light from the ellipsometer ($\geq 5 \times 8$ mm^2) were used to ensure that film nucleation was exclusively probed on the vdW surface. To omit optical interference and facilitate spectral modeling, we employed Si substrates with an ≈4 nm-thick silicon dioxide (SiO_2) layer, which also served to block charge transfer between Si and MoS_2. The SE data were modeled with a three-layer structure consisting of Si, SiO_2, and monolayer MoS_2 (Figure 1b, inset), which enabled changes in the dielectric function of MoS_2 to be determined as a function of growth parameters and time. Using the well-established dielectric functions of Si and SiO_2, along with the known parameters for the monolayer MoS_2 thickness (t_{MoS2} = 7 Å, measured by atomic force microscopy) and high-frequency permittivity ($\varepsilon_\infty = 6.1$),[17] the optical response of MoS_2 in the relevant spectral range is well described with four uncorrelated Tauc–Lorentz oscillators (Supporting Information S2),[18] characteristic of the A, B, C, and D excitons of monolayer MoS_2 (Figure 1b).[19] While the dominant optical transitions of MoS_2 occur in the range of 340–800 nm, the near-infrared spectral range (1100–1700 nm) exhibits a strong sensitivity to the thickness of growing AlO_x without a significant contribution from the 2D material (Figure S2, Supporting Information), thereby allowing simultaneous quantification of the excitonic properties of MoS_2 and the AlO_x thickness, as detailed in the Supporting Information S2.

We then applied the ellipsometric model to probe changes in the adsorbate thickness and the MoS_2 dielectric function in situ, during each stage of the ALD cycle, as well as across multiple cycles (Figure 1c,d). This study focuses on low-temperature (40 °C) ALD of alumina, which provides a benchmark material and is of relevance to 2D materials electronics. Such a low-temperature process is desired to enable the physisorption of TMA on the otherwise unreactive basal plane, while also avoiding the possibility of sulfur vacancy generation and suppressing deleterious side reactions of monolayer MoS_2 with ALD reactants. Ozone (O_3) was used as the oxidant instead of water because the latter easily forms a physisorbed multilayer at such low deposition temperatures. We note that at elevated temperatures (>100 °C), O_3 spontaneously decomposes into O_2 and oxygen radicals (O*), whereas it is stable at lower temperatures.[20] Importantly, there was no measurable change in the SE spectra after consecutive exposure of the MoS_2 to O_3 (Figure S3, Supporting Information), confirming that at the given reaction conditions (40 °C, $p_{O3} \approx 20$ Torr), there is little chemical interaction between O_3 and MoS_2. Similar to alumina growth on an oxidized substrate (e.g., Si/SiO_2), the measured thickness increased after the introduction of TMA and decreased after exposure to O_3 (Figure 1c), indicating the decomposition of methyl-ligands and the generation of hydroxylated surface groups suitable for reaction in the subsequent ALD cycle.[20–21] However, metal–organic precursor adhesion on the vdW surface is still weaker than on an initially hydroxylated surface and results in delayed nucleation on MoS_2 for the TMA/O_3 process (Figure 1c and Figure S4, Supporting Information).

We next examined the influence of the ALD film formation on the MoS_2 optical properties. By tracking ALD in real-time with in situ SE, we refined the growth parameters, including the precursor dose, background pressures, and purge times required to reach saturation after the introduction of gas-phase reactants. After dosing TMA, we observed a constant shift of the Δ spectrum without any measurable changes in Ψ (Figure S3, Supporting Information) or in the peak energies of the excitonic transitions associated with MoS_2 (Figure 1c). The observation that the exciton properties are not altered suggests the formation of a weakly interacting (physisorbed) molecular adsorbate layer that has a negligible impact on the dielectric environment and carrier concentration in MoS_2. However, after sequential exposure to both TMA and ozone, the characteristic exciton absorption peaks redshifted and the Δ signal decreased over the entire spectral range (Figure 1c and Figure S2, Supporting Information). The measured redshift and reduced strength of the extinction coefficient of MoS_2 (Figure 1d) after exposure to TMA and ozone suggest an increased carrier concentration associated with the formation of AlO_x.[22] While similar changes have been previously reported via ex situ measurements of MoS_2 monolayers capped with thicker AlO_x layers,[8d,23] our results shed light into the underlying mechanisms of these changes and their evolution during the early stages of film formation. In particular, the reduced intensities and red-shifts in the excitonic absorption features are resolved even after the very first TMA/O_3 cycle (Figure 1c). With subsequent cycles, the magnitudes of these changes increase stepwise, and eventually saturate at an AlO_x film thickness of ≈15 Å (Figure 1c and Figure S5, Supporting Information), which approaches the minimum thickness typically required to achieve a continuous oxide overlayer,[24] and accomplished here without the use of a detrimental plasma treatment. We note that the decreased strength of the B exciton feature after nine ALD cycles leads to significant fitting uncertainty, which manifests as apparent noise and drift of the plotted data. However, the saturation characteristics are well resolved via analysis of the C optical transition (Figure 1c).

The strong responsivity of the MoS_2 dielectric function to the initial TMA/O_3 cycles, as well as its saturation after repeated cycling (Figure S5, Supporting Information), indicates that changes to the excitonic absorption are dominated by interfacial processes, such as charge transfer doping (Figure S10, Supporting Information). Indeed, electrical transport measurements confirm the increase in electron concentration in MoS_2 monolayers following ALD deposition (Figure S11, Supporting Information). Importantly, these in situ SE measurements provide strong evidence that AlO_x adlayer-induced doping stems largely from the charge distribution directly at the MoS_2/AlO_x interface, as previously suggested by Pop and co-workers.[8d] As such, these results provide the intriguing opportunity to controllably adjust the carrier concentration in the 2D semiconductor with the ALD cycle number while maintaining an ultrathin coating within the length scale of charge carrier tunneling.

X-ray photoelectron spectroscopy (XPS) analysis confirmed the formation of aluminum oxide on continuous monolayer MoS_2 following ALD (Figure S6, Supporting Information). To assess how the TMA/O_3 process affects the chemistry of monolayer MoS_2, we compared X-ray photoelectron spectra of a bare monolayer of MoS_2 and a monolayer of MoS_2 capped with

© 2023 The Authors. Advanced Materials Interfaces published by Wiley-VCH GmbH

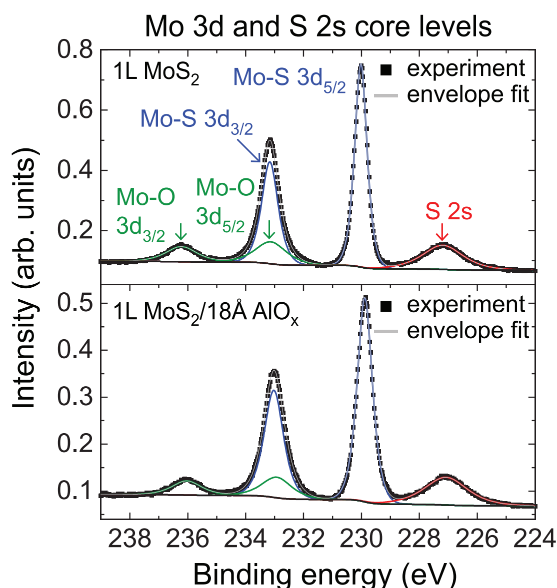

Figure 2. X-ray photoelectron spectroscopy of the Mo 3d core level region of continuous MoS_2 monolayers on Si/SiO_2 substrates without an ALD coating (top image) and with a nanometer-thin AlO_x layer (bottom image) deposited at 40 °C (12 cycles TMA/O_3). The photoelectron spectrum is well-approximated with one component for the S 2s core level (red) and two components, considering Mo-S (blue) and Mo-O (green) bonding, for the Mo 3d core level. To minimize charging during XPS, the sample was contacted with gold.

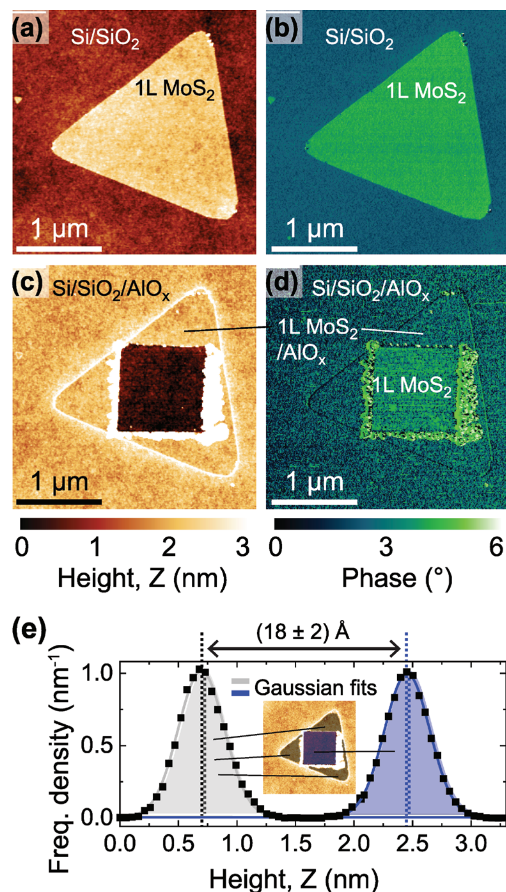

Figure 3. Intermittent-contact mode AFM topography (a,c) and phase images (b,d) of an isolated MoS_2 flake on a Si/SiO_2 substrate before (a,b) and after (c,d) encapsulation with AlO_x (12 cycles TMA/O_3). The AlO_x coating was removed within a 1 µm × 1 µm region in contact mode to determine its thickness and assess its bonding strength to the 2D material. e) The thickness of the ALD AlO_x coating was determined from the peaks positions of the Gaussian profiles used to approximate the height distributions extracted from the AFM height image shown in c. The inset shows the image in (c) with masked regions (grey and blue) considered for evaluation of the height distributions of AlO_x-coated and scratched MoS_2.

an 18 Å-thin AlO_x coating (**Figure 2**). To within the measurement error, these results reveal equal molybdenum to sulfur ratios (Mo:S) of 1:1.98 and 1:1.96 for the uncoated and the AlO_x-coated MoS_2 film, respectively (Table S2, Supporting Information). Importantly, the absence of nonstoichiometric Mo_xS_y peaks[25] in the photoelectron spectra suggests a physisorbed alumina adlayer on MoS_2 devoid of interface chemical bonds and without the introduction of lattice defects (e.g., sulfur vacancies), to within the measurement sensitivity. Noticeably, molybdenum trioxide (MoO_3) is present in both films at similar concentrations of 7.23% and 6.51% for the bare and AlO_x-coated MoS_2, respectively. The detected MoO_3 is characteristic of the commercially-obtained continuous monolayer MoS_2 films and likely stems from parasitic MoO_3 that crystallized on the growth substrate during CVD (Supporting Information S1, Supporting Information), as well as partial oxidation during prolonged air exposure. Nevertheless, we find that the ALD process reported here does not result in additional oxidation of monolayer MoS_2.

To elucidate the effect of the ultrathin AlO_x adlayer on the surface morphology and optoelectronic properties of MoS_2 at the micrometer scale, while also avoiding the typical inhomogeneities such as grain boundaries that characterize the continuous 2D film discussed above, we then utilized CVD-grown isolated monolayer MoS_2 flakes (Figure S1b, Supporting Information). As previously reported, such flakes are also characterized by an absence of MoO_3.[25] Atomic force microscopy images before and after encapsulation of the same monolayer MoS_2 flake (**Figure 3**) show a continuous and smooth ALD coating with a root mean square (rms) roughness, R_{rms}, of 2.2 Å, which agrees well with reported roughness values of AlO_x-coated MoS_2 on Si substrates.[24,26] Both monolayer MoS_2 and the AlO_x adlayer on the single layer sheet conform to the topography of the underlying Si/SiO_2 substrate (R_{rms} = 2.3 Å). The fact that the roughness did not increase following alumina deposition provides further support for the formation of a continuous AlO_x coating.

To determine the AlO_x thickness and examine the bonding strength of the ALD film to the MoS_2 monolayer, we performed contact mode AFM. Within a defined range of forces exerted by the AFM tip ($F_{ts} \geq 250$ nN), the ALD AlO_x film can be selectively removed from the MoS_2, as indicated by the restored phase contrast (Figure 3c,d) and optical properties (**Figure 4**). In comparison, substantially larger forces ($F_{ts} > 800$ nN) are required to abrade the AlO_x coating from the Si/SiO_2 substrate (Figure S8, Supporting Information). We note that much larger forces (>2 µN) were reported to scratch the MoS_2 itself.[27] The obtained thickness of the AlO_x layer on monolayer MoS_2 of

© 2023 The Authors. Advanced Materials Interfaces published by Wiley-VCH GmbH

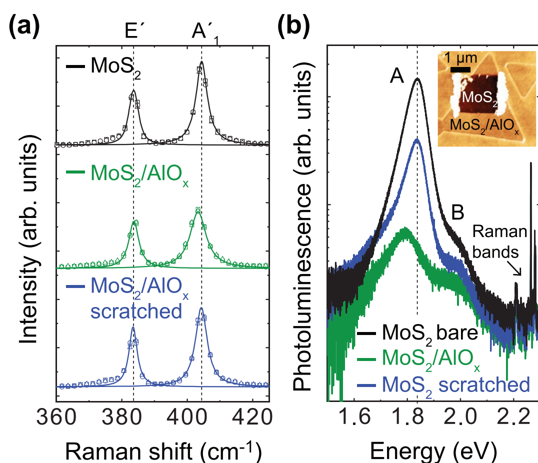

Figure 4. a) Raman spectra of different monolayer MoS_2 flakes before ALD (top), after deposition of an 18 Å-thin AlO_x layer (center), and after scratching off the AlO_x layer in a micrometer region of the flake (bottom). The spectra are vertically offset for clarity. The reversibility of the Raman peak positions indicates a weak interaction between the ALD AlO_x and MoS_2. b) Representative photoluminescence spectra of a bare, ALD-coated, and scratched monolayer MoS_2 flake. The inset shows an AFM topograph of a monolayer MoS_2 flake after AlO_x deposition and partial removal of the AlO_x within a 2×2 μm^2 area. The spectral features around 2.25 eV are Raman bands of Si and monolayer MoS_2.

~18 Å following 12 cycles of TMA and O_3 at 40 °C (Figure 3e) corresponds to an average growth-per-cycle (GPC) of 1.5 Å on the vdW surface and ≈2.2 Å on the SiO_2, which is similar to reported GPC of ≈2 Å on oxide surfaces for an ozone-based ALD AlO_x process at 30 °C.[28] The finding that AlO_x growth proceeds similarly on both continuous MoS_2 films, which possess MoO_3 impurities, and on MoS_2 flakes, which do not possess MoO_3 impurities, suggests that the presence of Mo oxides does not play a crucial role in the ALD process.

The weak interaction and damage-free removal of AlO_x off the 2D surface by contact mode AFM is further confirmed by Raman and photoluminescence (PL) spectroscopy measurements (Figure 4). Raman spectroscopy indicates an increase of the carrier concentration for the AlO_x-coated MoS_2.[29] In particular, we observed a significant redshift of the A'_1 mode, $\Delta\omega(A'_1)$ = -0.99 ± 0.19 cm^{-1}, which translates to an increase in the electron concentration of 4.4 ± 0.8×10^{12} cm^{-2},[29] for the AlO_x-coated monolayer MoS_2 (Figure 4a, green line) compared to the uncoated MoS_2 (Figure 4a, black line). Despite the small AlO_x thickness, the observed Raman shift is comparable to reported doping-related AlO_x-induced shifts in monolayer MoS_2 encapsulated with thicker AlO_x.[8d]

In addition to the changes of the A'_1 mode, the E' mode is blueshifted after MoS_2 monolayer capping with AlO_x. Because the E' mode of monolayer MoS_2 is nearly insensitive to changes in the carrier concentration,[29] its peak position and width allow for quantification of changes of strain within the monolayer, largely decoupled from changes in the carrier concentration. The observed shift of the E' mode is relatively minor ($\Delta\omega(E')$ = 0.19 ± 0.08 cm^{-1}) indicating negligible strain (<0.1%)[30] following encapsulation with AlO_x.

Comparing the PL spectra obtained before (Figure 4b, black line) and after AlO_x deposition (Figure 4b, green line) reveals an intensity decrease and a redshift of the MoS_2 A and B exciton emission lines (Table S3, Supporting Information). The observed changes in exciton luminescence are consistent with the spectral changes obtained by in situ SE (Figure 1) and suggest *n*-type doping of MoS_2[31] via charge transfer from the amorphous alumina adlayer, which has been reported to introduce electrons from occupied defect states within AlO_x (e.g., oxygen vacancies and hydrogen interstitials)[32] into the MoS_2 conduction band.[8d] Together with the immediate impact of AlO_x on the MoS_2 dielectric function measured by in situ SE, this finding highlights the important role of the interface on charge transfer and adlayer modulation doping.

Remarkably, physical removal of the AlOx adlayer using an AFM tip results in near-complete recovery of the MoS_2 Raman and PL spectra to their initial peak positions, linewidths, and intensities (Figure 4). These results provide further confirmation that the ALD AlO_x/MoS_2 interface reported here is characterized by weak electrostatic interactions at the 2D/3D interface. Indeed, the finding that AlO_x-induced changes to the optoelectronic properties of MoS_2 are reversible upon removal of the coating indicates that the ALD process does not introduce a significant concentration of defects into the MoS_2 and that few chemical bonds between MoS_2 and AlO_x are formed. Here, we note that the initial PL intensity was not fully restored after AlO_x removal. However, this can be explained with the finite lateral dimension of the scratched window (≈4 μm^2). While this size is larger than the size of the laser spot (≈0.6 μm^2), it is smaller than the area of exciton diffusion (≈7 μm^2), which we estimated with the reported neutral exciton diffusion length of 1.5 µm for monolayer MoS_2.[33] Thus some suppression of PL intensity is induced by the adlayer-doped regions outside the scratched window.

PL and Raman spectroscopy of individual monolayer MoS_2 flakes on Si/SiO_2 substrates further demonstrate the protective function of the nanometer-thin AlO_x layer during metallization (**Figure 5**). After evaporation of a 3 nm-thick gold (Au) layer directly onto monolayer MoS_2, the initially strong photoluminescence (Figure 5a, black line) is nearly completely quenched (Figure 5a, red line), which is consistent with prior findings.[34] In contrast, the PL signal for the AlO_x-protected MoS_2 with the gold layer atop is enhanced (Figure 5a, blue line) relative to the bare MoS_2 luminescence (Figure 5a, black line). The observed increase in the PL intensity can be explained with the electrostatic screening of charged defects within MoS_2 (e.g., vacancies) and the dielectric surrounding by the gold coating.[35] Additionally, the PL intensity of the gold-coated 2D material can increase through plasmonic enhancement,[36] though given the small thickness (3 nm) of the gold layer, this effect likely plays a minor role. For the case of the gold-capped alumina-coated MoS_2, the stronger dielectric screening reduces the band gap as a consequence of band gap renormalization, resulting in an additional red shift of the exciton peak energies (Table S3, Supporting Information).[37]

For the case of a 3 nm gold layer applied directly onto the surface of monolayer MoS_2 without AlO_x present (Figure 5b, red line), we observed a softening of both Raman modes as a consequence of strain (4.1%) and charge transfer effects,[38] as well as a splitting of the A'_1 mode, which has previously been attributed to the formation of gold islands on MoS_2.[39] Indeed,

© 2023 The Authors. Advanced Materials Interfaces published by Wiley-VCH GmbH

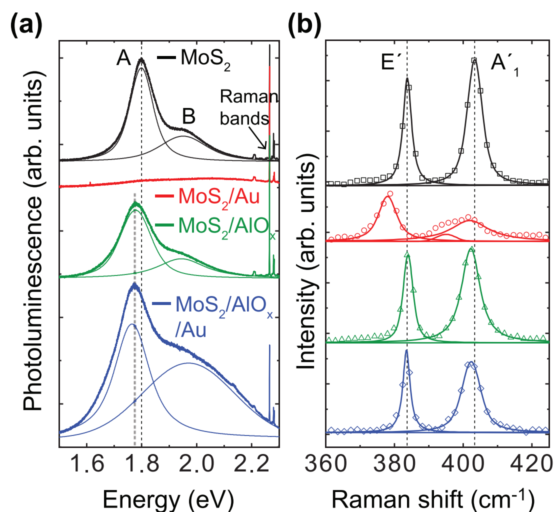

Figure 5. a) Photoluminescence spectra of a representative monolayer MoS_2 flake before (black line) and after evaporation of 3 nm of gold (red line). PL spectra of a monolayer MoS_2 flake, coated with a ≈1.8 nm-thick AlO_x layer (12 cycles TMA/O_3), before (green line) and after deposition of gold (blue line). The A and B exciton peaks are indicated in the figure. The spectral features around 2.25 eV are Raman bands of Si and monolayer MoS_2. b) Raman spectroscopy series of isolated monolayer MoS_2 flakes (same as shown in a) before (black squares) and after gold evaporation (red circles) on a bare MoS_2 flake, as well as before (green triangles) and after gold deposition (blue diamonds) on an AlO_x-protected MoS_2 monolayer. A 532 nm laser at 295.2 µW power, focused through a 50× objective, was used for the measurements. The spectra are plotted with a vertical offset for clarity.

the 3 nm thin gold coating forms a dense film of gold nanoparticles (Figure S9, Supporting Information) rather than a smooth and continuous layer. While it has been reported that reactions between gold and MoS_2 are energetically unfavorable,[40] strong interactions between Au und MoS_2 are commonly observed and can lead to interfacial Mo-S bond formation and introduce lattice defects[41] and introduce lattice defects.[6] Here, such strong interactions between Au and MoS_2 are observed, as indicated by the measured XPS linewidth broadening of the Mo 3d core levels (Figure S7, Supporting Information). In contrast, for the AlO_x-protected MoS_2 monolayer, the energy positions and linewidths of the Raman modes (Table S4, Supporting Information) are hardly affected by Au deposition, demonstrating protection of the 2D material from metal adlayer-induced strain in the metal-insulator-semiconductor (MIS) structure (Figure 5, blue line). Thus, the AlO_x adlayer allows the desirable optoelectronic properties of the MoS_2 to be maintained, even at the ultrathin limit, making it a highly effective encapsulant.

3. Conclusion

In summary, we demonstrated in situ SE on 2D semiconductors as a powerful method for simultaneously understanding film nucleation and its influence on the optoelectronic characteristics of the 2D material during ALD. Excitonic absorption in 2D materials is sensitive to lattice defects and changes in the carrier concentration, which could thus be probed in real time during alumina deposition on a continuous film of CVD-grown monolayer MoS_2 that was used as the model 2D semiconductor. Here, we find that charge transfer doping of the MoS_2 occurs from the very first cycle of AlO_x formation in the sub-monolayer regime and progresses with increasing cycle number. However, its saturation within the ultrathin film regime (~15 Å) points to a modulation doping mechanism defined directly at the MoS_2/AlO_x interface. From the insights gained by in situ SE, we applied an ALD process for the encapsulation of 2D materials with a weakly bonded (physisorbed), continuous, and ultrathin AlO_x layer at 40 °C. By implementing this AlO_x coating as a spacer layer, we prevented defect formation in the 2D crystal during metallization and enabled photoluminescence enhancement for the $Au/AlO_x/MoS_2$ system instead of quenching. Thus, the presented approach is promising for producing tunneling contacts or for seeding thicker dielectrics of relevance to the integration of 2D materials in electronic devices. Because the ALD process is not limited to the surface chemistry of MoS_2, the ultrathin alumina encapsulant can be applied as a general interlayer that facilitates integration of 2D materials with bulk materials. Beyond the demonstrated ALD process of this study, we highlight that in situ SE during deposition enables critical insights into the impact of film growth on the optoelectronic properties of 2D materials, starting from the very earliest stages of nucleation. Such an approach can thus greatly accelerate the development of new coatings and processes of relevance for controlling the properties of 2D materials and their integration into functional systems.

4. Experimental Section

Atomic Layer Deposition: MoS_2 was coated with AlO_x in a hot-wall ALD reactor (Fiji G2, Veeco CNT) in continuous flow mode. AlO_x films were grown using TMA (electronic grade, 99.999%, STREM Chemicals) as the precursor and Ar (99.9999%, Linde) as the carrier gas during the first half-cycle at ≈0.09 Torr. The reactor wall and chuck temperatures were controlled to 40 °C. Importantly, the thermal energy at 40 °C is below the O_3 decomposition energy and the heat of desorption for sulfur vacancies in MoS_2, thus substantially lowering the likelihood of undesired chemical reactions of the 2D surface in the presence of O_3.[42] During the second half-cycle, O_3 was remotely generated using oxygen (99.9999%, Linde) and supplied with 150 ms pulses and peak pressures of ≈20 Torr. Each cycle of the TMA/O_3 process followed the sequence: 0.1 s TMA dose, 30 s Ar purge, 0.1 s TMA dose, 30 s Ar purge, 0.15 s O_3 pulse. We note that we introduced two consecutive pulses of TMA to maximize the coverage of adsorbed TMA on MoS_2 by mitigating the effect of transient steric hinderances of the metal–organic molecules during precursor exposure.

Spectroscopic Ellipsometry: Changes in the aluminum oxide layer thickness and the MoS_2 dielectric function were monitored in real-time using an in situ spectroscopic ellipsometer (M-2000, J. A. Woollam) with a sampling time of ≈3 s during ALD. The light of a xenon lamp (Hamamatsu, L2174-01) was focused to a spot area of ≈5 × 8 mm^2 on the sample surface. The incoming and reflected light passed through fused silica windows (Lesker, VPZL-275DU) oriented in a fixed angle (≈67°) geometry. Details of the ellipsometric models for the bare and AlO_x-covered continuous monolayer films of MoS_2 on SiO_2-coated Si substrates are described in Supporting Information S2. To estimate the thickness of the adsorbate formed after TMA adsorption, an extra material layer was included in the model structure and was approximated with a Cauchy model. In the spectral range of the MoS_2

© 2023 The Authors. Advanced Materials Interfaces published by Wiley-VCH GmbH

bandgap (<800 nm), AlO_x adlayer formation affects both the surface optical properties and the MoS_2 excitonic absorption. By acquiring SE data in the visible and the near-infrared range (1000–1700 nm), in which there is no absorption by MoS_2, we were able to measure the optical properties and thickness of the adlayer independent from its effect on the MoS_2 optical properties (Figure S2, Supporting Information).

X-Ray Photoelectron Spectroscopy: XPS data were acquired in the hybrid lens mode at pass energy of 10 eV and a take-off angle of 0° with a Kratos Axis Supra setup equipped with a monochromatic Al Kα X-ray source (photon energy = 1486.7 eV) operated with an emission current of 15 mA. The beam area was set to ≈2 × 1 mm^2 using the slot collimation mode. The binding energy of the hemispherical analyzer was calibrated with in situ sputter-cleaned silver, gold, and copper standard samples. Thereby, the kinetic energies of the Ag 3d (1118.51 eV), Au 4f (1402.73 eV), and Cu 2p (554.07 eV) core levels were referenced with an accuracy of 25 meV to the known peak values. The instrumental broadening (0.30 eV) was determined by fitting of the measured Ag 3d core level spectrum of the silver calibration sample with a Voigt function.

Atomic Force Microscopy: AFM measurements were carried out with a Bruker Multimode V microscope (Billerica, MA, USA) in ambient conditions using NSG30 AFM probes (TipsNano) with a nominal tip radius of 8 nm, typical resonance frequency of 320 kHz, and force constant of 40 N m^{-1}. Height images over 10 × 10 μm^2 and 1 × 1 μm^2 scan windows were acquired at a scan rate of 0.5 Hz with 512-point sampling. The rms roughness was determined from 1 μm^2 images. The ultrathin ALD coating was removed from the surfaces of monolayer and multilayer MoS_2 using a PtSi-coated AFM tip (Nanosensors) in contact mode at forces < 100 nN. The tip-sample force, F_{ts}, in hard contact with the surface was calculated using Hooke's law, $F_{ts} = ks$, where the measured deflection, s, was determined from a force-distance curve and the spring constant, k, was obtained from a thermal tune.

Raman and Photoluminescence Spectroscopy: Raman and PL spectroscopy measurements were carried out using a 532 nm green laser with the excitation power was fixed at 295.2 µW. Spectra were acquired with a 50× objective and spectrally resolved with an 1800 grooves/mm grating using an inVia Reflex Raman spectroscopy setup (Renishaw, United Kingdom). Measured Raman spectra were referenced to the 520 cm^{-1} mode of the Si substrate. The PL spectra were collected with a 10 s integration time using Renishaw's SynchroScan method of acquiring wide-range spectra. PL and Raman peaks were approximated with Voigt functions.

Supporting Information

Supporting Information is available from the Wiley Online Library or from the author.

Acknowledgements

This work was supported by the DFG through the TUM International Graduate School of Science and Engineering (IGSSE), project FEPChem2D (16.01) and by the Deutsche Forschungsgemeinschaft (DFG, German Research Foundation) under Germany's Excellence Strategy – EXC 2089/1 – 390776260. The authors gratefully acknowledge the members of the Chair of Technical Electrochemistry from the Chemistry Department of the Technical University of Munich for measurement time at the XPS system. C.Q. gratefully acknowledges the Alexander von Humboldt Foundation for financial support in the framework of their fellowship program.

Open access funding enabled and organized by Projekt DEAL.

Conflict of Interest

The authors declare no conflict of interest.

Author Contributions

All authors have given approval to the final version of the manuscript.

Data Availability Statement

The data that support the findings of this study are available from the corresponding author upon reasonable request.

Keywords

2D materials integration, 2D materials protection, atomic layer deposition, in situ ellipsometry, monolayer MoS_2, ultrathin aluminum oxide

Received: December 3, 2022
Revised: February 18, 2023
Published online: April 18, 2023

[1] D. Deng, K. S. Novoselov, Q. Fu, N. Zheng, Z. Tian, X. Bao, *Nat. Nanotechnol.* **2016**, *11*, 218.
[2] Z. Sun, A. Martinez, F. Wang, *Nat. Photon.* **2016**, *10*, 227.
[3] Q. Qiu, Z. Huang, *Adv. Mater.* **2021**, *33*, 2008126.
[4] Y. Liu, X. Duan, H.-J. Shin, S. Park, Y. Huang, X. Duan, *Nature* **2021**, *591*, 43.
[5] International Roadmap for Devices and Systems (IRDS), https://www.irds.ieee.org/editions/2022 (accessed November **2022**).
[6] Y. Liu, J. Guo, E. Zhu, L. Liao, S.-J. Lee, M. Ding, I. Shakir, V. Gambin, Y. Huang, X. Duan, *Nature* **2018**, *557*, 696.
[7] a) S. J. McDonnell, R. M. Wallace, *JOM* **2019**, *71*, 224; b) H. Zhang, D. Chiappe, J. Meersschaut, T. Conard, A. Franquet, T. Nuytten, M. Mannarino, I. Radu, W. Vandervorst, A. Delabie, *J. Chem. Phys.* **2017**, *146*, 052810.
[8] a) S. A. Wells, A. Henning, J. T. Gish, V. K. Sangwan, L. J. Lauhon, M. C. Hersam, *Nano Lett.* **2018**, *18*, 7876; b) W. C. Shin, T. Y. Kim, O. Sul, B. J. Cho, *Appl. Phys. Lett.* **2012**, *101*, 033507; c) G. Lin, M.-Q. Zhao, M. Jia, J. Zhang, P. Cui, L. Wei, H. Zhao, A. T. C. Johnson, L. Gundlach, Y. Zeng, *J. Phys. D: Appl. Phys.* **2019**, *53*, 105103; d) C. J. McClellan, E. Yalon, K. K. H. Smithe, S. V. Suryavanshi, E. Pop, *ACS Nano* **2021**, *15*, 1587; e) S. Kim, J. Nah, I. Jo, D. Shahrjerdi, L. Colombo, Z. Yao, E. Tutuc, S. K. Banerjee, *Appl. Phys. Lett.* **2009**, *94*, 062107; f) W. Li, J. Zhou, S. Cai, Z. Yu, J. Zhang, N. Fang, T. Li, Y. Wu, T. Chen, X. Xie, H. Ma, K. Yan, N. Dai, X. Wu, H. Zhao, Z. Wang, D. He, L. Pan, Y. Shi, P. Wang, W. Chen, K. Nagashio, X. Duan, X. Wang, *Nat. Electron.* **2019**, *2*, 563.
[9] a) L. Cheng, X. Qin, A. T. Lucero, A. Azcatl, J. Huang, R. M. Wallace, K. Cho, J. Kim, *ACS Appl. Mater. Interfaces* **2014**, *6*, 11834; b) C. Jung, H. I. Yang, W. Choi, *Nanoscale Res. Lett.* **2019**, *14*, 278.
[10] a) Q. Qian, B. Li, M. Hua, Z. Zhang, F. Lan, Y. Xu, R. Yan, K. J. Chen, *Sci. Rep.* **2016**, *6*, 27676; b) Y. Song, Y. He, Y. Li, H. Wei, P. Qiu, Q. Huang, Z. He, J. Die, M. Peng, X. Zheng, *Cryst. Growth Des.* **2021**, *21*, 1778; c) J. Jang, Y. Kim, S.-S. Chee, H. Kim, D. Whang, G.-H. Kim, S. J. Yun, *ACS Appl. Mater. Interfaces* **2020**, *12*, 5031.
[11] a) K. M. Price, S. Najmaei, C. E. Ekuma, R. A. Burke, M. Dubey, A. D. Franklin, *ACS Appl. Nano Mater.* **2019**, *2*, 4085; b) J. A. Kropp, A. Sharma, W. Zhu, C. Ataca, T. Gougousi, *ACS Appl. Mater. Interfaces* **2020**, *12*, 48150.
[12] J. Y. Shang, M. J. Moody, J. Chen, S. Krylyuk, A. V. Davydov, T. J. Marks, L. J. Lauhon, *ACS Appl. Electron. Mater.* **2020**, *2*, 1273.

© 2023 The Authors. Advanced Materials Interfaces published by Wiley-VCH GmbH

[13] a) A. Azcatl, Q. Wang, M. J. Kim, R. M. Wallace, *APL Mater.* **2017**, *5*, 086108; b) H. Zhu, R. Addou, Q. Wang, Y. Nie, K. Cho, M. J. Kim, R. M. Wallace, *Nanotechnology* **2019**, *31*, 055704; c) J. H. Park, H. C. P. Movva, E. Chagarov, K. Sardashti, H. Chou, I. Kwak, K.-T. Hu, S. K. Fullerton-Shirey, P. Choudhury, S. K. Banerjee, A. C. Kummel, *Nano Lett.* **2015**, *15*, 6626; d) H. Zhu, S. McDonnell, X. Qin, A. Azcatl, L. Cheng, R. Addou, J. Kim, P. D. Ye, R. M. Wallace, *ACS Appl. Mater. Interfaces* **2015**, *7*, 13038.

[14] a) Y.-S. Lin, J.-Y. Hoo, T.-F. Chung, J.-R. Yang, M.-J. Chen, *ACS Appl. Electron. Mater.* **2020**, *2*, 1289; b) Y.-S. Lin, P.-H. Cheng, K.-W. Huang, H.-C. Lin, M.-J. Chen, *Appl. Surf. Sci.* **2018**, *443*, 421; c) I. Kwak, M. Kavrik, J. H. Park, L. Grissom, B. Fruhberger, K. T. Wong, S. Kang, A. C. Kummel, *Appl. Surf. Sci.* **2019**, *463*, 758; d) S. Jandhyala, G. Mordi, B. Lee, G. Lee, C. Floresca, P.-R. Cha, J. Ahn, R. M. Wallace, Y. J. Chabal, M. J. Kim, L. Colombo, K. Cho, J. Kim, *ACS Nano* **2012**, *6*, 2722.

[15] a) H. Liu, K. Xu, X. Zhang, P. D. Ye, *Appl. Phys. Lett.* **2012**, *100*, 152115; b) S.-J. Jeong, H. W. Kim, J. Heo, M.-H. Lee, H. J. Song, J. Ku, Y. Lee, Y. Cho, W. Jeon, H. Suh, S. Hwang, S. Park, *2D Mater.* **2016**, *3*, 035027.

[16] a) A. Valsaraj, J. Chang, A. Rai, L. F. Register, S. K. Banerjee, *2D Mater.* **2015**, *2*, 045009; b) M. Weidner, A. Fuchs, T. J. M. Bayer, K. Rachut, P. Schnell, G. K. Deyu, A. Klein, *Adv. Funct. Mater.* **2019**, *29*, 1807906.

[17] A. Laturia, M. L. Van de Put, W. G. Vandenberghe, *npj 2D Mater. Appl.* **2018**, *2*, 6.

[18] G. A. Ermolaev, Y. V. Stebunov, A. A. Vyshnevyy, D. E. Tatarkin, D. I. Yakubovsky, S. M. Novikov, D. G. Baranov, T. Shegai, A. Y. Nikitin, A. V. Arsenin, V. S. Volkov, *npj 2D Mater. Appl.* **2020**, *4*, 21.

[19] a) C. Trovatello, H. P. C. Miranda, A. Molina-Sánchez, R. Borrego-Varillas, C. Manzoni, L. Moretti, L. Ganzer, M. Maiuri, J. Wang, D. Dumcenco, A. Kis, L. Wirtz, A. Marini, G. Soavi, A. C. Ferrari, G. Cerullo, D. Sangalli, S. D. Conte, *ACS Nano* **2020**, *14*, 5700; b) G. A. Ermolaev, D. I. Yakubovsky, Y. V. Stebunov, A. V. Arsenin, V. S. Volkov, *J. Vac. Sci. Technol. B* **2020**, *38*, 014002.

[20] S. D. Elliott, G. Scarel, C. Wiemer, M. Fanciulli, G. Pavia, *Chem. Mater.* **2006**, *18*, 3764.

[21] D. N. Goldstein, J. A. McCormick, S. M. George, *J. Phys. Chem. C* **2008**, *112*, 19530.

[22] B. Song, H. Gu, M. Fang, Z. Guo, Y.-T. Ho, X. Chen, H. Jiang, S. Liu, *ACS Appl. Electron. Mater.* **2021**, *3*, 2564.

[23] S. Y. Kim, H. I. Yang, W. Choi, *Appl. Phys. Lett.* **2018**, *113*, 133104.

[24] B. Huang, M. Zheng, Y. Zhao, J. Wu, J. T. L. Thong, *ACS Appl. Mater. Interfaces* **2019**, *11*, 35438.

[25] T. Grünleitner, A. Henning, M. Bissolo, M. Zengerle, L. Gregoratti, M. Amati, P. Zeller, J. Eichhorn, A. V. Stier, A. W. Holleitner, J. J. Finley, I. D. Sharp, *ACS Nano* **2022**, *16*, 20364.

[26] E. Schilirò, R. L. Nigro, S. E. Panasci, S. Agnello, M. Cannas, F. M. Gelardi, F. Roccaforte, F. Giannazzo, *Adv. Mater. Interfaces* **2021**, *8*, 2101117.

[27] A. Özoğul, F. Trillitzsch, C. Neumann, A. George, A. Turchanin, E. Gnecco, *Phys. Rev. Mater.* **2020**, *4*, 033603.

[28] S. K. Kim, S. W. Lee, C. S. Hwang, Y.-S. Min, J. Y. Won, J. Jeong, *J. Electrochem. Soc.* **2006**, *153*, F69.

[29] B. Chakraborty, A. Bera, D. V. S. Muthu, S. Bhowmick, U. V. Waghmare, A. K. Sood, *Phys. Rev. B* **2012**, *85*, 161403.

[30] a) Y. Y. Hui, X. Liu, W. Jie, N. Y. Chan, J. Hao, Y.-T. Hsu, L.-J. Li, W. Guo, S. P. Lau, *ACS Nano* **2013**, *7*, 7126; b) C. Rice, R. J. Young, R. Zan, U. Bangert, D. Wolverson, T. Georgiou, R. Jalil, K. S. Novoselov, *Phys. Rev. B* **2013**, *87*, 081307.

[31] S. Mouri, Y. Miyauchi, K. Matsuda, *Nano Lett.* **2013**, *13*, 5944.

[32] O. A. Dicks, J. Cottom, A. L. Shluger, V. V. Afanas'ev, *Nanotechnology* **2019**, *30*, 205201.

[33] S. Z. Uddin, H. Kim, M. Lorenzon, M. Yeh, D.-H. Lien, E. S. Barnard, H. Htoon, A. Weber-Bargioni, A. Javey, *ACS Nano* **2020**, *14*, 13433.

[34] U. Bhanu, M. R. Islam, L. Tetard, S. I. Khondaker, *Sci. Rep.* **2014**, *4*, 5575.

[35] a) T. L. Atallah, J. Wang, M. Bosch, D. Seo, R. A. Burke, O. Moneer, J. Zhu, M. Theibault, L. E. Brus, J. Hone, X. Y. Zhu, *J. Phys. Chem. Lett.* **2017**, *8*, 2148; b) T. Grünleitner, A. Henning, M. Bissolo, A. Kleibert, C. A. F. Vaz, A. V. Stier, J. J. Finley, I. D. Sharp, *Adv. Funct. Mater.* **2022**, *32*, 2111343.

[36] a) S. Najmaei, A. Mlayah, A. Arbouet, C. Girard, J. Léotin, J. Lou, *ACS Nano* **2014**, *8*, 12682; b) M. Garai, Z. Zhu, J. Shi, S. Li, Q.-H. Xu, *J. Chem. Phys.* **2021**, *155*, 234201.

[37] N. Peimyoo, H.-Y. Wu, J. Escolar, A. De Sanctis, G. Prando, F. Vollmer, F. Withers, A. C. Riis-Jensen, M. F. Craciun, K. S. Thygesen, S. Russo, *ACS Appl. Mater. Interfaces* **2020**, *12*, 55134.

[38] S. Sarkar, P. Kratzer, *J. Phys. Chem. C* **2021**, *125*, 26645.

[39] a) C. Gong, C. Huang, J. Miller, L. Cheng, Y. Hao, D. Cobden, J. Kim, R. S. Ruoff, R. M. Wallace, K. Cho, X. Xu, Y. J. Chabal, *ACS Nano* **2013**, *7*, 11350; b) K. Schauble, D. Zakhidov, E. Yalon, S. Deshmukh, R. W. Grady, K. A. Cooley, C. J. McClellan, S. Vaziri, D. Passarello, S. E. Mohney, M. F. Toney, A. K. Sood, A. Salleo, E. Pop, *ACS Nano* **2020**, *14*, 14798.

[40] C. M. Smyth, R. Addou, S. McDonnell, C. L. Hinkle, R. M. Wallace, *J. Phys. Chem. C* **2016**, *120*, 14719.

[41] Y. Huang, Y.-H. Pan, R. Yang, L.-H. Bao, L. Meng, H.-L. Luo, Y.-Q. Cai, G.-D. Liu, W.-J. Zhao, Z. Zhou, L.-M. Wu, Z.-L. Zhu, M. Huang, L.-W. Liu, L. Liu, P. Cheng, K.-H. Wu, S.-B. Tian, C.-Z. Gu, Y.-G. Shi, Y.-F. Guo, Z. G. Cheng, J.-P. Hu, L. Zhao, G.-H. Yang, E. Sutter, P. Sutter, Y.-L. Wang, W. Ji, X.-J. Zhou, et al., *Nat. Commun.* **2020**, *11*, 2453.

[42] D. Liu, Y. Guo, L. Fang, J. Robertson, *Appl. Phys. Lett.* **2013**, *103*, 183113.

 © 2023 The Authors. Advanced Materials Interfaces published by Wiley-VCH GmbH